

## Article

# Effect of a Control Mechanism on the Interaction between a Rectangular Jet and a Slotted Plate: Experimental Study of the Aeroacoustic Field

Nour Eldin Afyouni <sup>1</sup>, Marwan Alkheir <sup>2</sup> , Hassan Assoum <sup>3,\*</sup> , Bilal El Zohbi <sup>1</sup>, Kamel Abed-Meraim <sup>1</sup>, Anas Sakout <sup>1</sup> and Mouhammad El Hassan <sup>4,\*</sup> 

<sup>1</sup> LASIE UMR CNRS 7356, University of La Rochelle, 17000 La Rochelle, France; nour.afyouni@univ-lr.fr (N.E.A.); bilal.zohbi@outlook.com (B.E.Z.); kamel.abed-meraim@univ-lr.fr (K.A.-M.); asakout@univ-lr.fr (A.S.)

<sup>2</sup> UFEID Lab, Université Française d’Égypte, Caire 11837, Egypt; marwan.alkheir@ufe.edu.eg

<sup>3</sup> Mechanical Engineering Department, Beirut Arab University, Beirut P.O. Box 11-5020, Lebanon

<sup>4</sup> Mechanical Engineering Department, Prince Mohammad Bin Fahd University, Al Khobar 31952, Saudi Arabia

\* Correspondence: h.assoum@bau.edu.lb (H.A.); melhassan@pmu.edu.sa (M.E.H.)

**Abstract:** The aeroacoustic field of a rectangular subsonic jet impinging on a slotted plate was investigated experimentally using microphones and stereoscopic particle image velocimetry (S-PIV). The study was carried out with a Reynolds number of 6700 and an impact distance of 4 cm. The current configuration represents a benchmark standpoint, featuring high levels of generated noise. A control mechanism consisting of a thin rod was introduced downstream from the jet exit to suppress the self-sustained tones. A total of 1085 positions of the rod between the jet exit and impinging plate were tested to identify positions of optimal noise reduction. Two zones were distinguished in terms of control efficacy: a zone where the sound pressure level (SPL) dropped by up to 19 dB and another zone where the SPL increased by up to 14 dB. The velocity fields show that the presence of the rod divides the jet into two lateral secondary jets on both sides of the main jet axis. The outer part of the secondary jets expanded radially with less interaction with the plate compared to the case without the control. This behavior affected the deformation of vortices against the slot. Proper orthogonal decomposition was applied to the velocity field for a better understanding of the turbulence dynamics with and without the control rod.

**Keywords:** acoustic comfort; rectangular jet; SPIV; passive control; aeroacoustics



**Citation:** Afyouni, N.E.; Alkheir, M.; Assoum, H.; El Zohbi, B.; Abed-Meraim, K.; Sakout, A.; El Hassan, M. Effect of a Control Mechanism on the Interaction between a Rectangular Jet and a Slotted Plate: Experimental Study of the Aeroacoustic Field. *Fluids* **2023**, *8*, 309. <https://doi.org/10.3390/fluids8120309>

Academic Editor: D. Andrew S. Rees

Received: 25 August 2023

Revised: 21 November 2023

Accepted: 22 November 2023

Published: 28 November 2023



**Copyright:** © 2023 by the authors. Licensee MDPI, Basel, Switzerland. This article is an open access article distributed under the terms and conditions of the Creative Commons Attribution (CC BY) license (<https://creativecommons.org/licenses/by/4.0/>).

## 1. Introduction

Impinging jets are found in several industrial applications, such as the cooling of electronic parts, heating, ventilation air conditioning systems, and drilling processes, among others. In certain configurations, the impingement of a jet on a solid surface may generate whistles with a considerably high acoustic level. The sounds—called “Self-sustaining tones”—emitted from the impact are due to the pressure fluctuations produced with a fundamental frequency  $f$ . The pressure waves travel upstream towards the jet exit, modify the shear layer, and act with the vortical structures created near the jet exit. This mechanism is called an aeroacoustic feedback loop [1–7] (see Figure 1).

The feedback mechanism was discussed for the first time by Powell [8], who presented a mathematical model of the aeroacoustics field for an impinging jet based on Lighthill models [9–11], and explained that the presence of the edge in the flow direction creates a fluctuating force which is considered a dipole. This dipole disturbs the jet and creates instability with a gain factor depending on the jet characteristics (Reynolds number and Strouhal number). Then, Powell and Chanaud [12] studied experimentally two particular configurations of the edge tones: the first was an axisymmetric jet impinging on a flat plate

with a hole (hole tones), and the second was the impingement on a ring (ring tones). They found that the edge tone theory is applicable to the hole and ring tones with two differences: the first is in the directivity of the sound, and the second is in the region of occurrence in the Re-St diagram. Rockwell and Naudascher [13] presented the different configurations that produce the self-sustaining tones and summarized the previous work performed on each configuration.

Ho and Nosseir [14] focused on the feedback loop in a high-speed axisymmetric impinging jet with a small impact distance. Based on the near-field pressure measurements, it was proved that the feedback mechanism is responsible for the pressure fluctuations that produce the self-sustaining tones. In addition, the authors specify that the feedback loop is composed of two components, one obtained by the downstream convection of large-scale coherent structures, and the second from the impingement of the vortices of the plate, which produce waves that propagate upstream and excite the shear layer near the jet exit.

Krothapalli et al. [15] examined a supersonic impinging jet. Different impact distances were studied to find the effect of the impingement on the acoustic level. It was found that the presence of a solid plate increased the acoustic level by 8 dB as compared to a free jet. The results of the velocity field obtained from PIV measurements proved that coherent structures have the most important role in acoustic emission. The authors concluded that the prediction of noise production needs a better understanding of the convection velocity of large-scale vortices in the shear layer. In the same context, Mehta et al. [15] studied a supersonic rectangular impinging jet with  $Ma = 1.44$ . They found a similarity with the axisymmetric jet in terms of the coherent structures and sharp acoustic waves, meaning that Powell's model can also be applied to a rectangular jet. However, a rectangular jet was found to change the oscillation mode, and the acoustic tones were obtained by a combination of these different mode frequencies.

Furthermore, Zhang [16] gave more attention to the turbulent structures in a turbulent reacting impinging jet. It was found that the turbulence generator and the shear layer both had a significant effect on the generation of vortices. The small structures were found to be dependent on the turbulence generator and the fuel-to-air ratio. Acoustically, the author showed that the turbulence generator did not affect the acoustic characteristics of a cold jet; however, the combustion had a significant influence on sound emissions.

Uzun et al. [17] presented a numerical model to predict the acoustic noise generation of a supersonic-impinging jet. They found a strong dependency between the Reynolds number and the acoustic frequency.

El Hassan [18] studied the vortex dynamics in a circular impinging jet using TR-PIV measurements. Two Reynolds numbers were tested. Further attention was given to the wall shear stress distribution on the impinging plate. It was found that the wall shear stress was influenced by both the primary and the secondary vortices.

Assoum et al. [19–24] studied the configuration of a rectangular jet impinging on a slotted plate (slot tones) using stereoscopic and tomographic particle image velocimetry techniques. The authors showed that the sound emission was obtained by energy transfer from the aerodynamic to the acoustic modes and that the aerodynamic modes directly affected the self-sustained frequencies. A strong correlation between the acoustic frequencies and the dynamic modes, obtained from the dynamic mode decomposition (DMD) [25], was also found.

Previous studies have shown that coherent structures are responsible for sound emission in impinging jets. The control of acoustic noise is then based on the control of the vortex dynamics of the jet. Lucas et al. [26] studied noise reduction in a twin-jet nozzle utilizing flexible filaments and proved that they effectively eliminated screech tones and decreased the overall sound pressure level by more than 3 dB. Geyer [27] studied the efficacy of porous materials in the reduction in rectangular jet noise by introducing a porous cylinder cover in the flow direction. It was discovered that utilizing materials with low airflow resistivity resulted in a significant decrease in flow noise.

For active flow control methods, Alvi et al. [28] placed a circular array that consisted of supersonic microjets 400  $\mu\text{m}$  in diameter around the periphery of the main jet. This technique led to a reduction by about 8 dB in the near-field noise. A similar approach was proposed by Choi et al. [29], who investigated the effectiveness of two microjet control techniques: the first method involved a constant microjet injection, while the second method employed a pulsed microjet injection, driven by the goal to enhance noise attenuation. Kopiev et al. [30] studied experimentally how plasma actuators, based on surface barrier high-frequency discharge, affect jet noise characteristics and showed that, when  $St \approx 0.5$ , jet excitation led to a broadband amplification of jet sound radiation. However, for  $St > 2$ , jet excitation led to a noise reduction if the action was sufficiently intensive. The self-sustaining sounds control was also considered by many others studies [31–47]

Despite the study of some control techniques, the problem of noise reduction in impinging jets requires more effort to find better strategies. We therefore studied a passive control mechanism consisting of a 4 mm diameter rod installed between the jet exit and the impinging plate. The aeroacoustics of the rectangular subsonic impinging jet was experimentally investigated with and without a control. Both the acoustic signal and the velocity field were measured simultaneously using microphones and combined-SPIV, respectively. The jet configuration consisted of a rectangular air jet impinging on a slotted plate, with an impact ratio of  $L/H = 4$ , where  $L$  is the distance between the plate and the nozzle, and  $H$  is the height of the nozzle. The jet was an oscillating jet with  $St = f_0 H / U_0 = 0.17$  and  $Re = HU_0 / \nu = 6700$  (where  $f_0$  is the jet frequency,  $H$  is the jet exit height,  $U_0$  is the longitudinal velocity at the jet exit measured at the center of the jet). The Mach number was about 0.03. The choice of the Reynolds number is justified by the dramatically high acoustic noise. In order to find the optimal position of the rod, the zone between the jet exit and the slotted plate was swept with a 1 mm step along the  $X$  and  $Y$  axes; thus, a total of 1085 rod positions were tested.

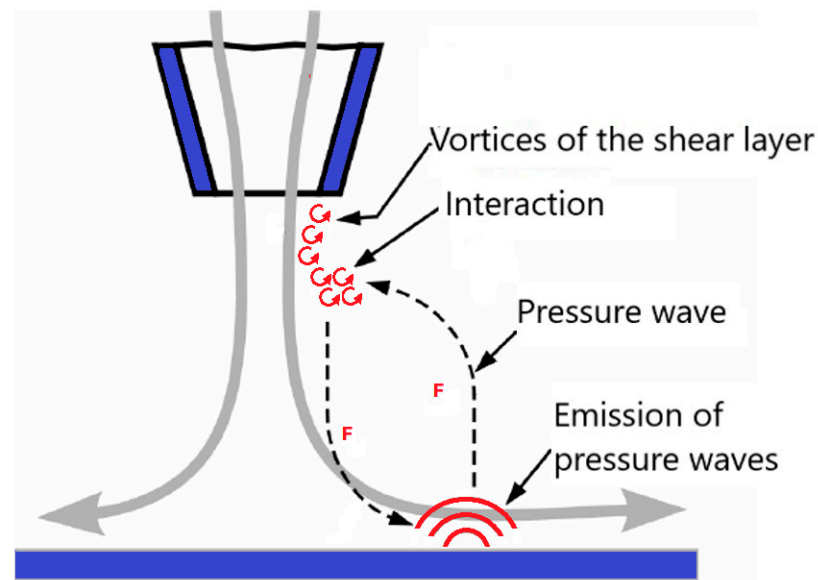


**Figure 1.** Schematic illustration of the feedback loop mechanism [48].

## 2. Materials and Methods

The experimental setup shown in Figure 2 consists of a compressor placed outside the experimental room. This compressor is controlled by a frequency chopper (Siemens MICROMASTER 420, three-phases) which was used to vary the outlet velocity up to 33 m/s ( $M \approx 0.1$ ), which means that the jet remained subsonic. The pulsed air passes through a large enclosure ( $V = 1 \text{ m}^3$ ) equipped with grids that serve to parallelize the flow streamlines and decrease the turbulence before the ejection of the airflow into a 1250 mm long duct with a 190 mm  $\times$  90 mm rectangular section. The rectangular section contained honeycombs to

parallelize the air streamlines before they arrived at a 4th-degree polynomial form nozzle. The height and width of the nozzle exit were  $H = 10\text{ mm}$  and  $L_z = 190\text{ mm}$ , respectively. The aspect ratio of the jet was  $l_z/H = 19$ . The jet coming out from the nozzle strikes a  $250\text{ mm} \times 250\text{ mm}$  slotted aluminum plate that was  $4\text{ mm}$  thick. This plate was provided with a slot of the same size as the jet outlet ( $H = 10\text{ mm}$ ,  $L_z = 190\text{ mm}$ ). The slot was beveled at  $45^\circ$  downstream and aligned with the nozzle. The impact distance  $L$  between the jet outlet and the plate was 4 times the nozzle height. Thus, the dimensionless distance  $L/H = 4$  was used in the rest of this study. The air was absorbed from a room just adjacent to the experimental room, in which the temperature was controlled and could vary between  $18 \leq T \leq 20^\circ\text{C}$ . To analyze how the position of the rod affects noise emission, we required particular fixation and displacement systems for regulating the rod's location. Utilizing a "LabVIEW" control program, the rod could move in both  $x$  and  $y$  directions. The  $x$ -direction movements ranged from  $X = -15\text{ mm}$  (below the jet) to  $X = 15\text{ mm}$  (above the jet). However, for the  $y$ -direction, the movements were limited. The rod began at  $Y = 3\text{ mm}$  with a  $2\text{ mm}$  radius and  $1\text{ mm}$  initial safety distance. It then moved to the edge of the slotted plate at  $Y = 37\text{ mm}$  with a  $2\text{ mm}$  radius and  $1\text{ mm}$  safety distance. The rod occupied a horizontal range of  $-15\text{ mm} \leq X \leq 15\text{ mm}$  and  $3\text{ mm} \leq Y \leq 37\text{ mm}$ , totaling to 1085 positions (see Figure 3a).

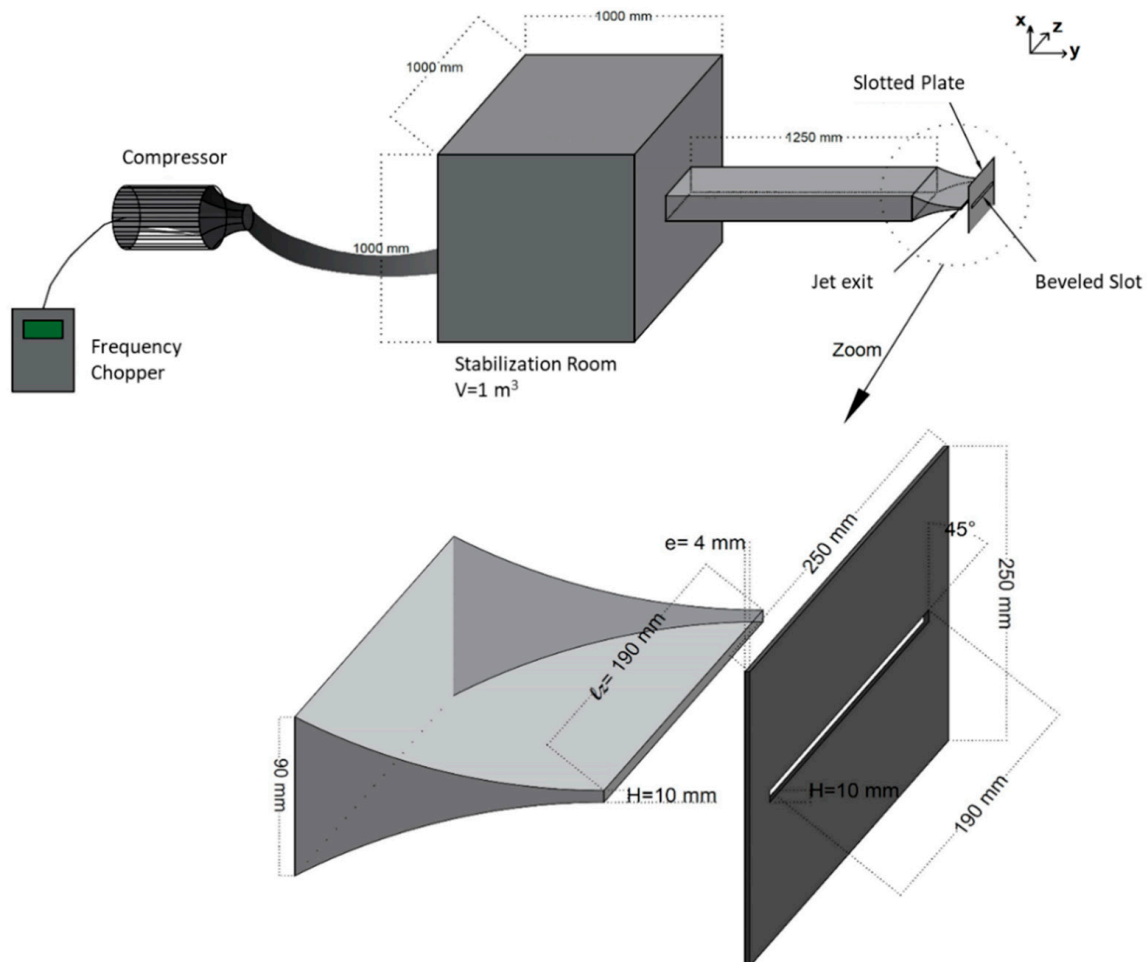
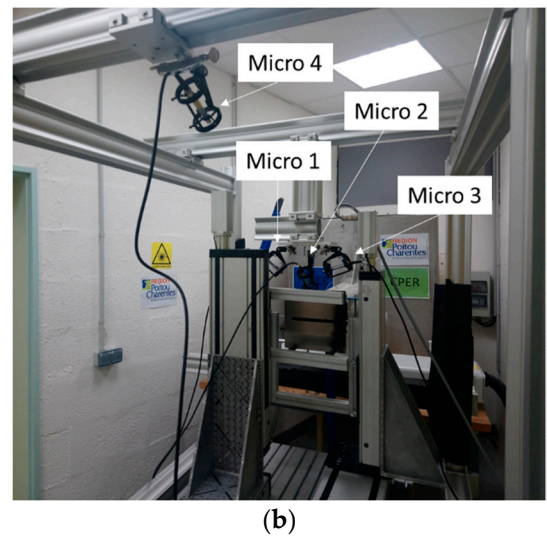
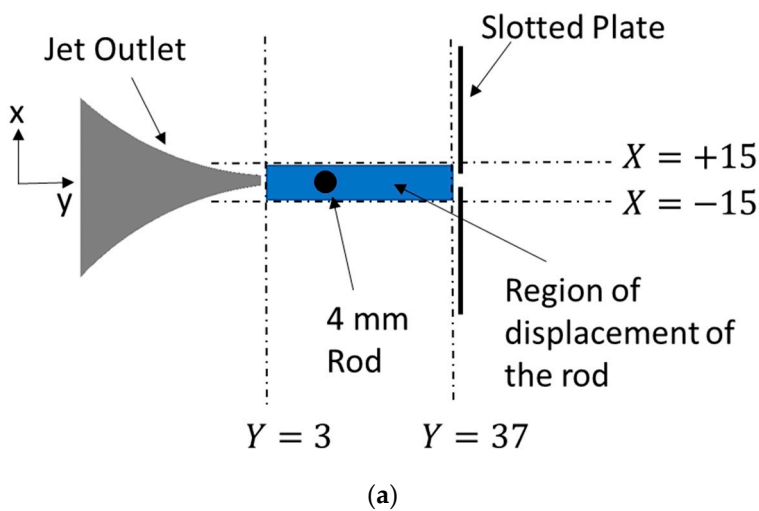


Figure 2. Schematic representation of the experimental setup.



**Figure 3.** (a) Illustration of the region of displacement of the rod (the dimensions are not real) and (b) photos that show the position of the microphones.

For the acoustic measurements, four microphones of type “4189 B&K” were used: the first was placed in the middle of the plate (below the slot) to avoid perturbing the flow) at a 15 cm distance behind the plate. The second and third microphones were positioned on either side of the first microphone at a distance of 25 cm from the plate. Finally, the fourth microphone was placed 2 m from the plate to measure the far field noise (see Figure 3b). The microphones were pre-polarized with a bandwidth of  $20 \leq f \leq 20$  kHz and their acoustic level measurement ranges were between 15.2 dB and 146 dB. The acoustic measurements were carried out with a sampling frequency of 15 kHz. These acoustic signals were acquired by NI LabVIEW 2019 software installed on a NI PXI 1036 National Instruments workstation equipped with a NI PXI 4496 dynamic card. Acoustic acquisition was synchronized with the S-PIV measurement using LabVIEW, so the two acquisitions were made simultaneously. Once a total of 1085 acoustic acquisitions had been carried out, these signals were processed on MATLAB V18 in order to calculate the sound pressure level. In addition, a spectral analysis using the FFT function was performed to understand the effect of the rod on the frequency activities.

The sounds produced upon flow impact with the slotted plate are a result of vortex formations. These structures can be identified through the use of the combined stereoscopic particle image velocimetry technique (C-SPIV) [49–53]. Olive oil was utilized as a tracer to seed the flow through an oil particle generator with an oil-air atomizer sprayed via the “Laskin Nozzle” aerographic system, as offered by “Lavision”. The lighting system utilized a Nd: YLF LDY 304-PIV Litron laser equipped with two 30 mJ/pulse heads operating at 1 kHz frequency and emitting a wavelength of  $\lambda = 527$  nm. The laser arm carried the beam to the area between the jet nozzle and the plate, passing through 7 mirrors with 96% transmission capability. The beam was transformed into a laser sheet by a sheet generator produced by “Lavision”. Thus, the web’s thickness and opening angle were tailored to the divergent lens utilized with a 10 mm focal length, which was selected to withstand the laser’s high light power. A mechanical laser delimiter was used to cut off the laser sheet at the jet nozzle, and the plate to reduce reflections. Acquisition was made in double frame acquisition mode, which means that the cameras took two frames at the desired sampling frequency. The duration between the two Dt frames was independent of the sampling frequency and needs to be chosen based on jet velocity and the camera’s position. In this experiment, Dt was 100  $\mu$ s. 2000 image pairs were acquired with a sampling frequency of 2.5 kHz. Synchronization between the laser pulses and the camera apertures was controlled by a high-speed controller (HSC) produced by Lavision. More details about the C-SPIV technique can be found in [54]. Once the images were acquired, a simple

pre-processing routine was applied to eliminate the noise of the cameras and homogenize the images. A standard SPIV algorithm was applied to the preprocessed images using Davis 10.1.0 software, allowing us to obtain the velocity fields. Several tests were made to find the maximum possible spatial resolution that gave a good correlation value. The calculation was made by windowing the image by  $16 \times 16$  square pixels with 50% overlap. Then, the spatial resolution was set at 8 pixels (0.76 mm). After finishing the calculation, a post-processing routine consisting of eliminating the vectors with a correlation value lower than 0.4 was applied. The obtained velocity field was filled by interpolation. In our configuration, the uncertainty on the values of each component of the velocity is estimated to be less than 5% [55]

### 3. Results

The sound pressure level distribution as a function of rod position is shown in Figure 4, depicting the average acoustic pressure measurements gathered from four microphones across 1085 positions of the rod. Note that the SPL values obtained from the microphones were found to be similar. For a Reynolds number of 6700 with an impact ratio of  $L/H$  equal to 4, the self-sustaining sound produced a sound pressure level of  $Lp = 83$  dB in the absence of a rod. Figure 4 presents three different zones: the first, marked in blue, experienced flow disturbance due to the presence of a rod, leading to a reduction in the sound pressure level,  $Lp$ , which could reach up to 19 dB. This zone had the same height as the nozzle and was located on either side of the jet's axis of symmetry. The symmetry decreases starting at a distance of  $H$  from the nozzle outlet. Nevertheless, the control effectiveness remains considerable up to a distance of  $Y/H = 2.6$  from the jet exit. The second area (orange and dark yellow) corresponds to a rise in the sound level, which could reach up to +14 dB. This area was not symmetrical with respect to the jet's axis. It occupied a longitudinal space of about 28 mm from the jet's outlet and the vertical positions ranged from approximately  $-0.65 < X/H < -0.45$ . It is worth noting that this zone gradually extended in a non-symmetrical manner from the longitudinal position  $Y/H = 1.5$  to  $Y/H = 3$ . Additionally, there was a minor area on the plate that indicated a slightly significant rise in the acoustic field. The third area was situated away from zones 1 and 2, where the rod did not interfere with the projected acoustic field. In this particular location, the acoustic frequency characteristics were identical to those observed without the presence of a rod.

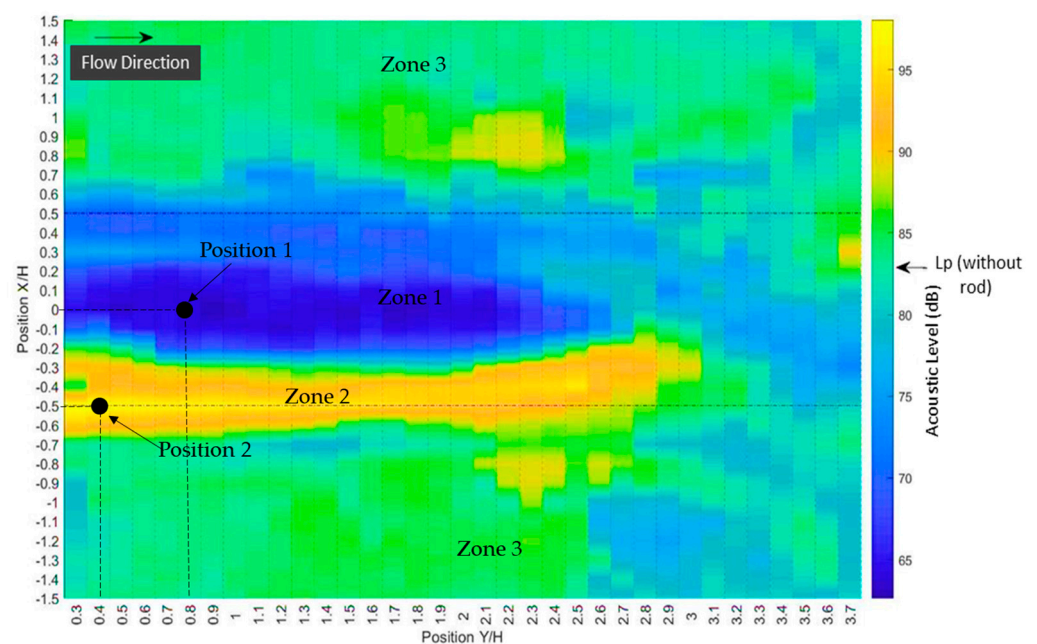


**Figure 4.** Sound pressure level at different rod locations for a  $Re = 6700$  and impact ratio  $L/H = 4$ .

To understand the effect of the rod on flow dynamics, as well as on noise production, acoustic and PIV data were used. The normalized mean velocity components ( $V_y/U_0$ ), and the root mean square ( $V_{rms}/U_0$ ), are shown in Figures 5 and 6, respectively. They show that the presence of a rod divided the main jet in two. These jets were symmetrical when a rod was placed in the center of the jet (position 1) and asymmetrical when a rod was in position 2. The statistical results do not provide an explanation for the noise production. For that, the instantaneous field will be considered in the rest of this study to examine the vortical structures.

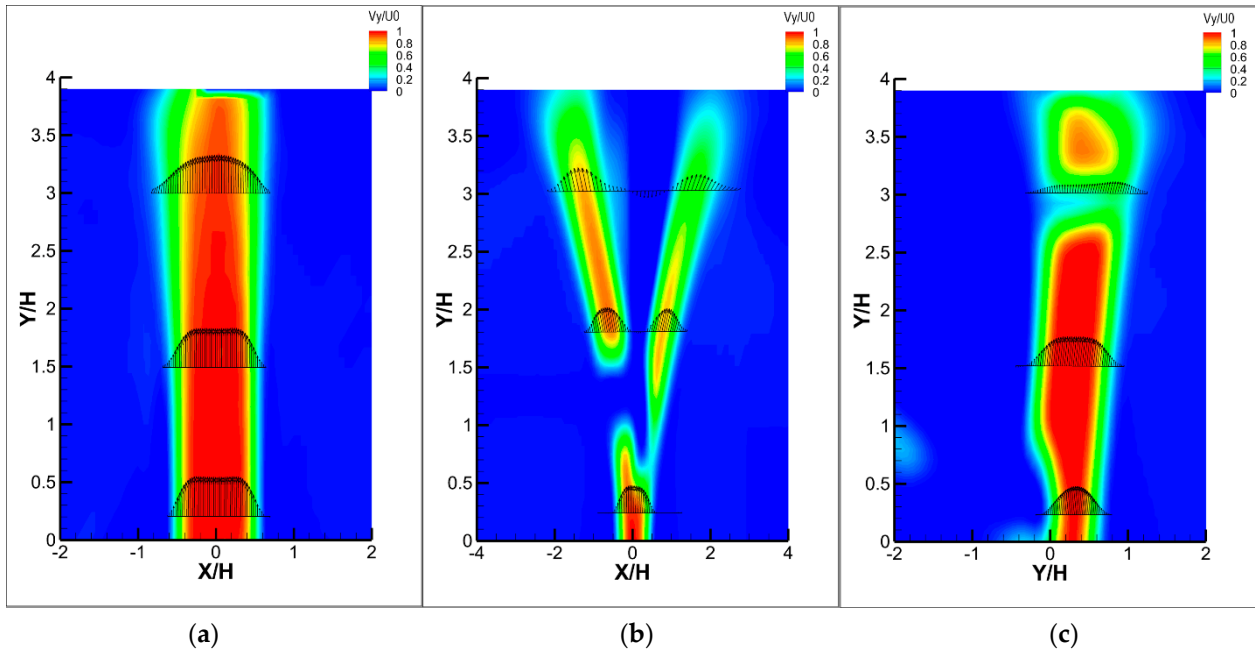


Figure 5. Mean longitudinal velocity field (a) the absence of a rod, (b) the rod occupies position 1, and (c) the rod occupies position 2.

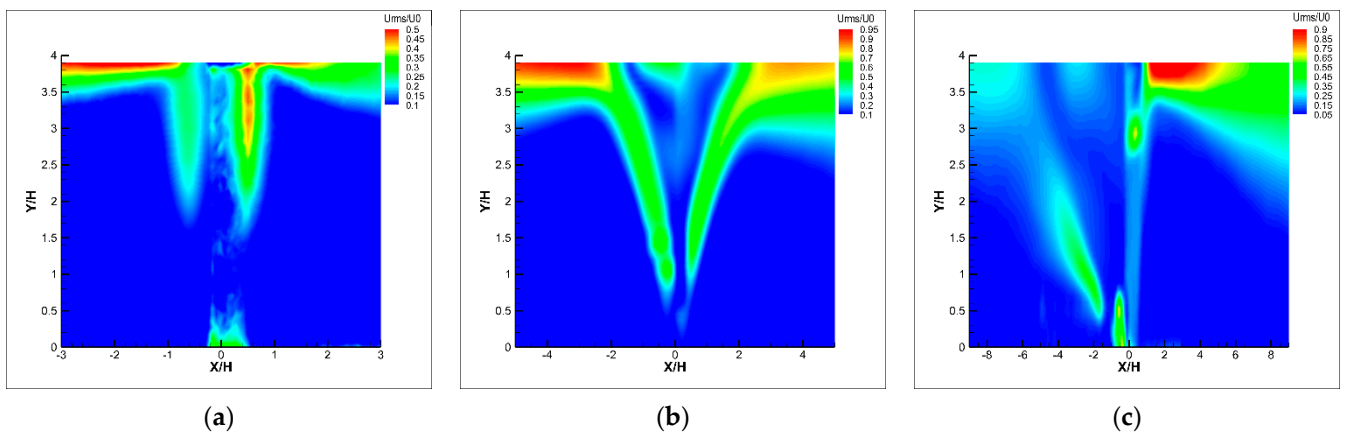
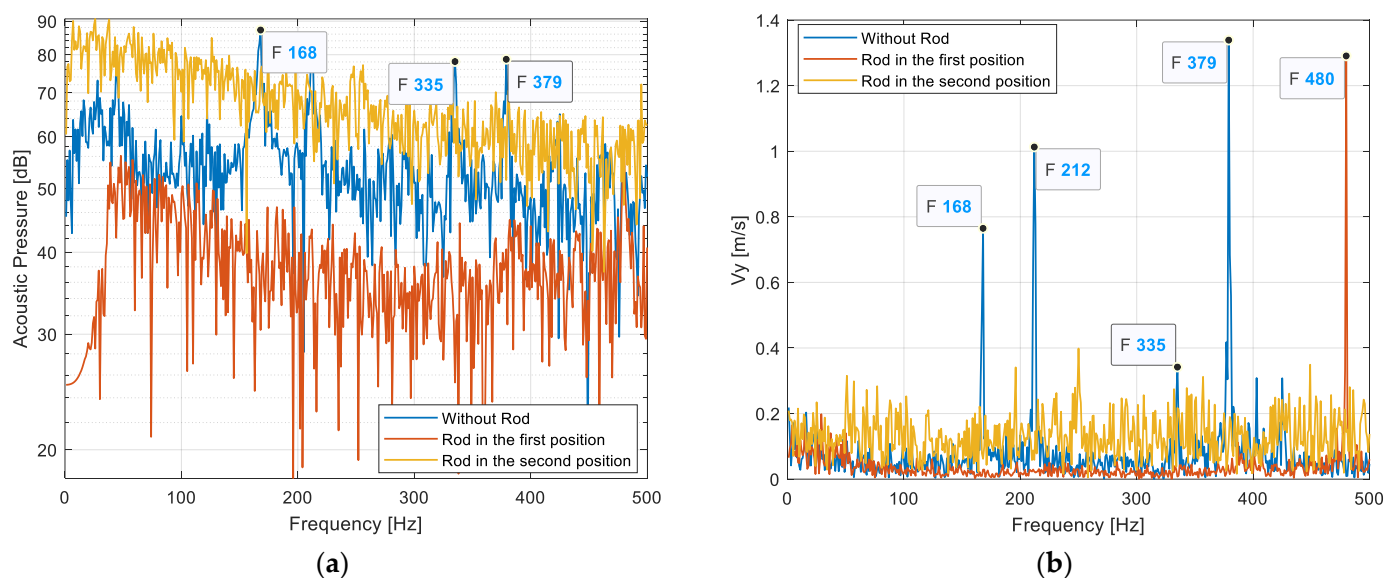


Figure 6. Root-mean-square longitudinal velocity (a) in the absence of a rod, (b) the rod occupies position 1, and (c) the rod occupies position 2.

A spectral analysis was performed to study the acoustic frequencies in the presence and absence of a rod. A fast Fourier transform was applied to both acoustic and velocity signals. Two random positions of a rod in the different zones were chosen to extract the velocity signal: ( $X/H = 0, Y/H = 0.8$ ) and ( $X/H = -0.5, Y/H = 0.4$ ) (see Figure 4), which are located in zones 1 and 2, respectively. It was found that the presence of a rod in these positions was accompanied by a reduction of 19.3 dB and an increase of 8.6 dB, respectively.

Figure 7a shows that in the absence of a rod, the acoustic spectrum had four peaks that correspond to the main frequency of 168 Hz and its higher order harmonic 335 Hz, 212 Hz and 379 Hz. When the rod was in the first position, the amplitudes of the acoustic signal decreased and the broadband spectrum was weak. As a result, the sound pressure level was reduced by 19.3 dB. When the rod was in the first position, the amplitude of all frequency peaks decreased and the broadband spectrum was weak. In contrast, when the rod was placed in the second position, all frequency peaks vanished, leading to self-sustaining sound loops. Furthermore, Figure 7a displays a broad frequency range with significant high amplitudes when the rod is positioned second, accounting for the 8.6 dB rise in sound pressure level. Figure 7b shows the spectrum of the longitudinal velocity signal, which was obtained by applying a FFT on the velocity signal extracted from the PIV results at a point of passage of the large-scale vortices. The spectrum without a rod had the same frequencies as the acoustic spectrum (168 Hz, 212 Hz, and 379 Hz), which confirms the aeroacoustic coupling. However, when the rod occupied the first position, the spectrum had one peak at 480 Hz; this frequency could correspond to a dynamic behavior that does not produce an acoustic wave.



**Figure 7.** (a) Acoustic pressure spectrum (logarithmic scale) and (b) longitudinal velocity spectrum, in the absence of a rod, in the presence of a rod at position 1, and in the presence of a rod at position 2.

In order to understand the origin of the variation in the velocity spectrum, the  $\lambda_2$  criteria [56] were calculated from the velocity field obtained from SPIV measurements as follows:

$$\lambda_2 = (S_{11} - S_{22})^2 + (S_{11} - S_{33})^2 + (S_{22} - S_{33})^2 + 4S_{12}^2 + 4S_{13}^2 + 4S_{23}^2$$

where  $S_{11}$ ,  $S_{22}$ , and  $S_{33}$  are the diagonal elements of the velocity gradient tensor, representing the rate of change of the velocity in the x, y, and z directions, respectively.  $S_{12}$ ,  $S_{13}$ , and  $S_{23}$  are the off-diagonal elements of the velocity gradient tensor, representing the rate of shear in different directions. The  $\lambda_2$  criterion identifies regions in the flow where the value of  $\lambda_2$  is negative [57]. Lagrangian vortex detection criteria have also been proposed in the literature [58] and can be implemented in future studies. Figure 8a,b show the instantaneous field of  $\lambda_2$  criterion and the vortex trajectories (obtained by a superposition of 100 snapshots) in three cases: the absence of a rod (1), the presence of a rod in position 1 (2), and the presence of a rod in position 2 (3). The arrangement of the vortices when no rod was installed showed that large structures move upstream in an anti-symmetrical arrangement (alternative way) and one vortex reached the slot at a specific instant t. The trajectory of

these structures indicates that the vortices interacted with the slot border and split into two parts: the first part passed through the slot and the second part impacted the surface of the plate and then travelled along the impinging wall. When the rod was in position 1, it divided the main jet symmetrically into two: the upper jet (on the positive X side) and the lower jet (on the negative X side). These jets displayed an antisymmetric character that dominated the vortex organization. Additionally, each jet had two paths. The first path was where vortices travelled along the wall in the transverse direction. The second path was formed by the trajectories of large coherent structures colliding with the plate wall, creating strong vortex activity and forming two recirculation zones on either side of the slot, without passing through it. This accounts for the absence of frequency peaks in the acoustic spectrum. The presence of a frequency of 480 Hz could correspond to the vortex shedding of the cylinder, which did not seem to couple with any acoustic frequencies. To verify this hypothesis, the local Strouhal number was calculated based on the rod diameter. It was found that the  $St_{f=480} = 0.19$ . The typical range for a circular cylinder is 0.15–0.3, which confirms the proposed hypothesis. In the second position of the rod, there was no vortex activity in the lower jet, whereas the flow of the upper jet exhibited an anti-symmetrical arrangement. The coherent structures in the lower part of the upper jet passed through the slot with minimal interaction with the slot edge, resulting in no feedback loop. This eliminates the self-sustaining tones and explains the absence of the energy frequency in the acoustic spectrum.

POD (proper orthogonal decomposition) and DMD (dynamic mode decomposition [57,59–63]) are two different procedures that can be used in order to obtain a deeper understanding of the jet dynamics. In this work, further analysis of the flow characteristics with and without a control were carried out using (POD) [61,64–70] applied to the PIV results. Figure 9 represents the kinetic energy (KE) distribution of different POD modes for  $Re = 6700$  in the absence of a rod (a) when the rod occupied the first position (b), and when the rod occupied the second position (c), for the 2000 modes calculated. Also, the cumulative energy (CE) sum was added to the plot. The results show that in the absence of a rod, the first 370 modes contained 90% of the total kinetic energy. The first two highest energy modes contained 25% of the total KE. In the presence of the rod at position 1, the first 115 modes contained 90% of the total KE. The first two highest energy modes contained 14% of the total KE. In the presence of the rod at position 2, the first 115 modes contained 90% of the total KE. The first two highest energy modes contained 20% of the total KE. The difference between the KE contained in the first two modes is related to the presence of the coherent structures in each case. In the absence of a rod, the large-scale structures were dominant and less chaotic (which was not the case when the rod was added, as shown in Figure 8). Then, in this case, fewer modes were needed to construct the mean flow (more energy was present in the first two modes compared to when the rod was present).

In their POD study on a jet impinging at different nozzle-to-plate ratios varying between one and eight, Milanovic and Hammad [63] showed that the first five highest energy modes contained between 19% and 32% of the total KE. At  $H/D \leq 4$  the vortices along the impingement wall were found to be most prominent. At higher nozzle-to-plate distances ( $H/D = 8$ ), the dominant flow structures were found to be along the periphery of the jet.

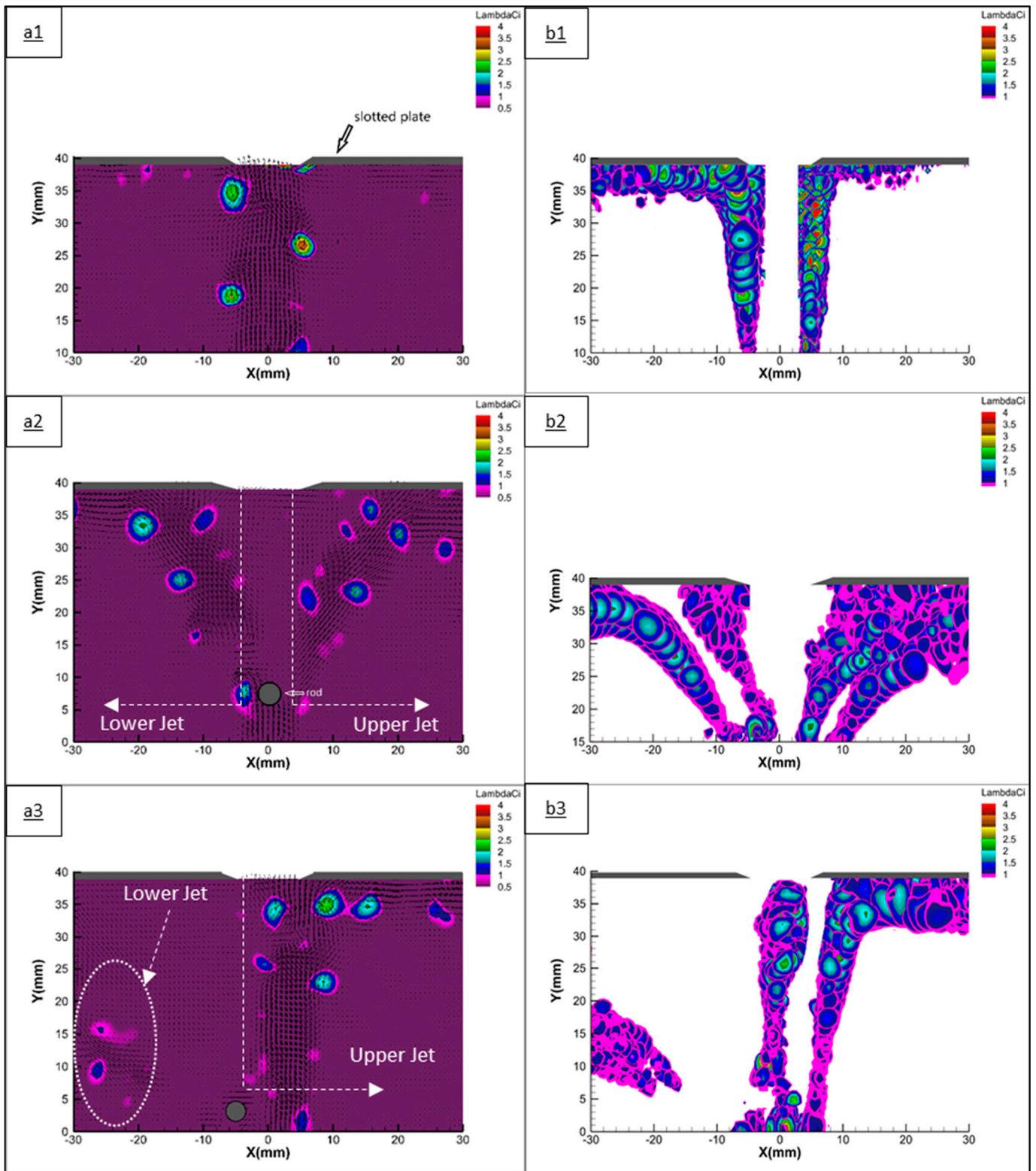


**Figure 8.** (a1) Instantaneous fields of  $\lambda_2$  criterion in the absence of the rod, (a2) Instantaneous fields of  $\lambda_2$  criterion in the presence of the rod in position 1, (a3) Instantaneous fields of  $\lambda_2$  criterion in the presence of the rod in position 2, (b1) vortex trajectory of 100 snapshots in the absence of the rod, (b2) vortex trajectory of 100 snapshots in the presence of the rod in position 1, (b3) vortex trajectory of 100 snapshots in the presence of the rod in position 2.

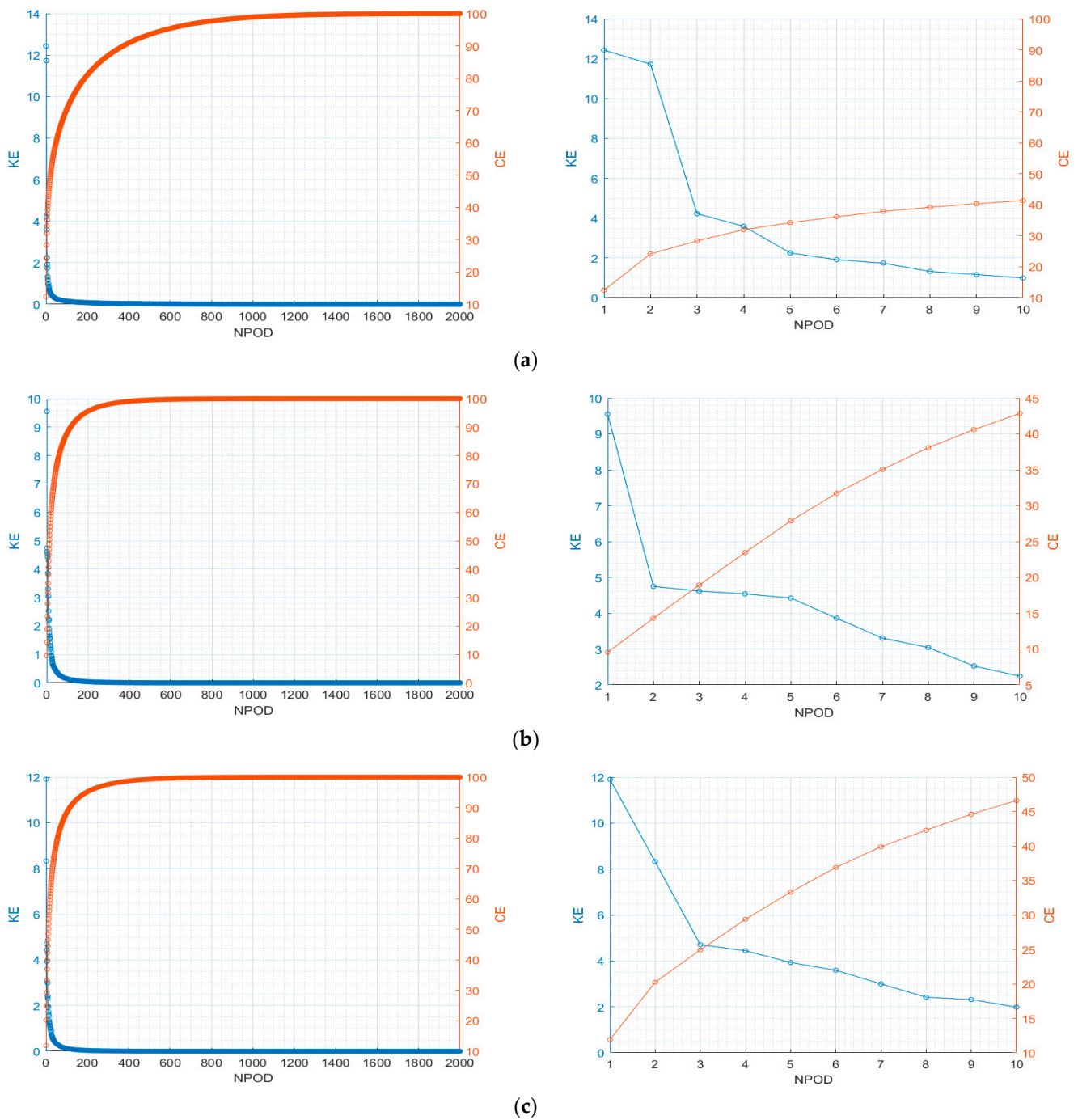


**Figure 9.** Kinetic energy of different POD spatial modes for  $Re = 6700$  in (a) the absence of a control, (b) with the rod at position 1, and (c) with the rod at position 2.

Figure 10 shows the first five highest energy modes of the longitudinal velocity in the absence of a control. Modes 1 and 2 present the vortex structures on both sides of the jet. These vortices hit the slotted plate before escaping through it. The second path, where the vortices deviated along the wall in the transverse direction, is shown by modes 3, 4, and 5. Also, these modes show the secondary vortices formed at the wall.

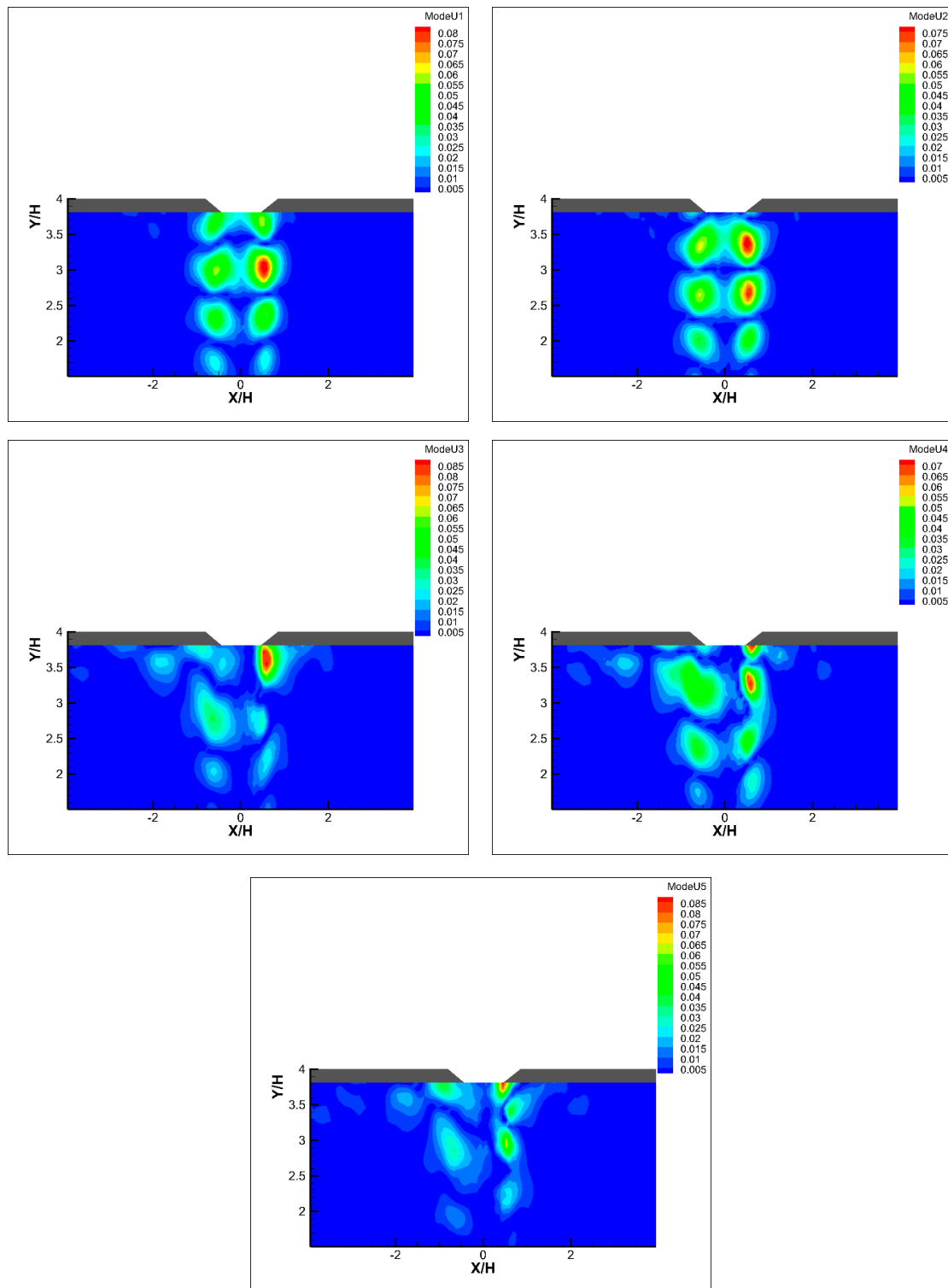


**Figure 10.** The first five highest energy spatial modes of longitudinal velocity ( $U_y$ ) were obtained by snapshot POD for  $Re = 6700$  in the absence of a control.

Figure 11 presents the first five highest energy modes for  $Re = 6700$  when the rod occupied position 1. The vortices that detached after flow impingement with the rod were found to be most prominent. As seen on the figure representing the vortex trajectory, the rod divided the main jet into two sub-jets. Mode 1 shows the two sub-jets, where the vortices followed two paths. The first is where the vortices deviated along the wall in the transverse direction and the second is where the vortices struck the wall of the plate.

Moreover, the strong vortex activity created two recirculation zones on either side of the slot. This mechanism was observed in all five modes. Modes 2, 3, 4 and 5 also showed the trajectories of vortices in addition to the secondary vortices near the plate.

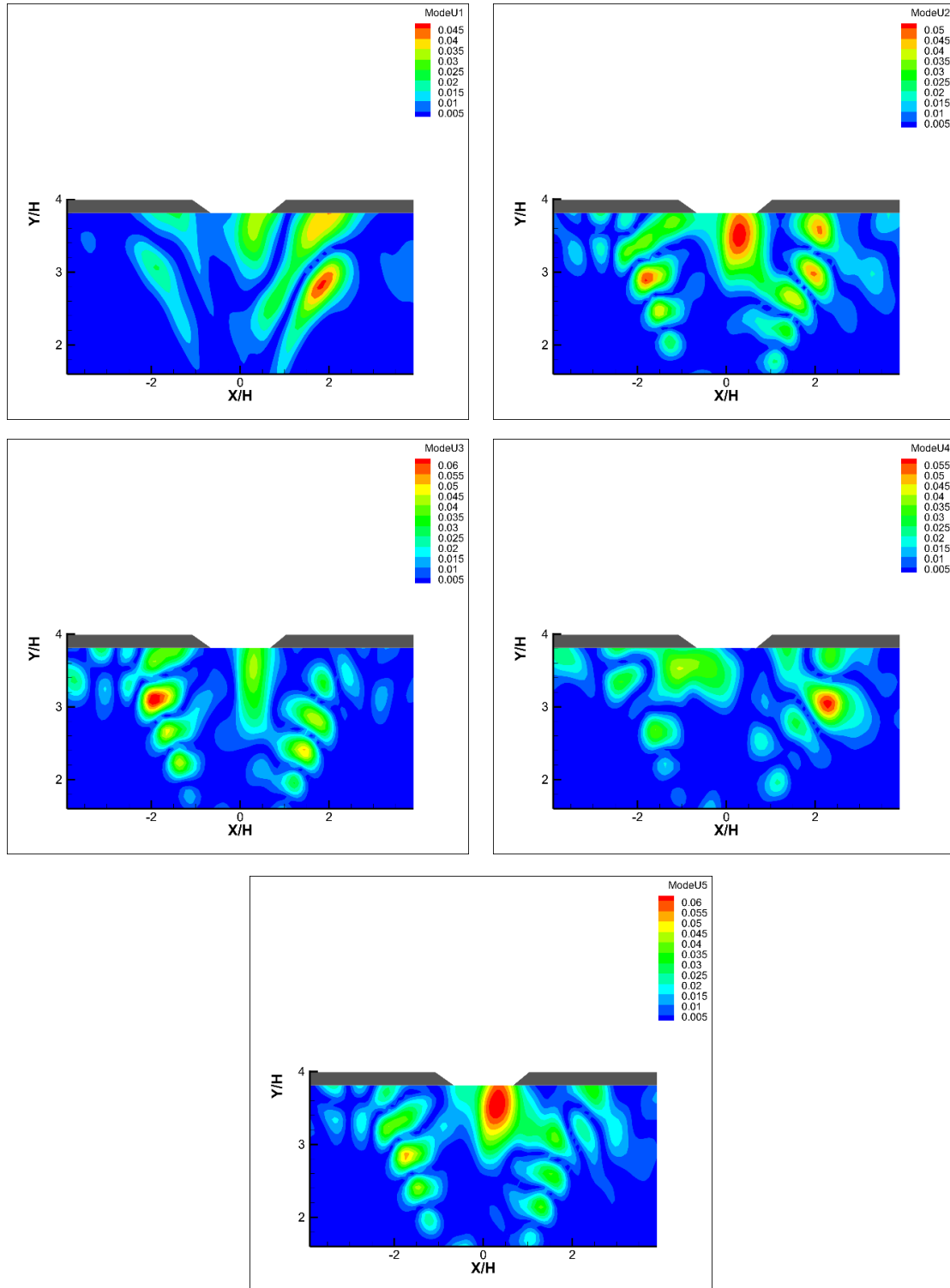


**Figure 11.** The first five highest energy spatial modes of longitudinal velocity ( $U_y$ ), obtained by snapshot POD for  $Re = 6700$  when the rod is at position 1.

The first five highest energy modes for  $Re = 6700$  when the rod occupied position 2 are shown in Figure 12. Mode 1 showed a vortex activity that detached after the flow interacted

with the rod. Modes 2, 3, and 4 showed the trajectory followed by the vortices. On the first path the vortices escaped through the slot, which led to the disappearance of the pressure waves created due to vortex impingement with the solid wall. On the second path the vortices travelled along the wall in the transverse direction. Mode 5 showed the secondary vortices that formed at the impingement wall. We recommend that the POD be used to highlight the many important flow dynamics responsible for the acoustic generation in impinging jets.

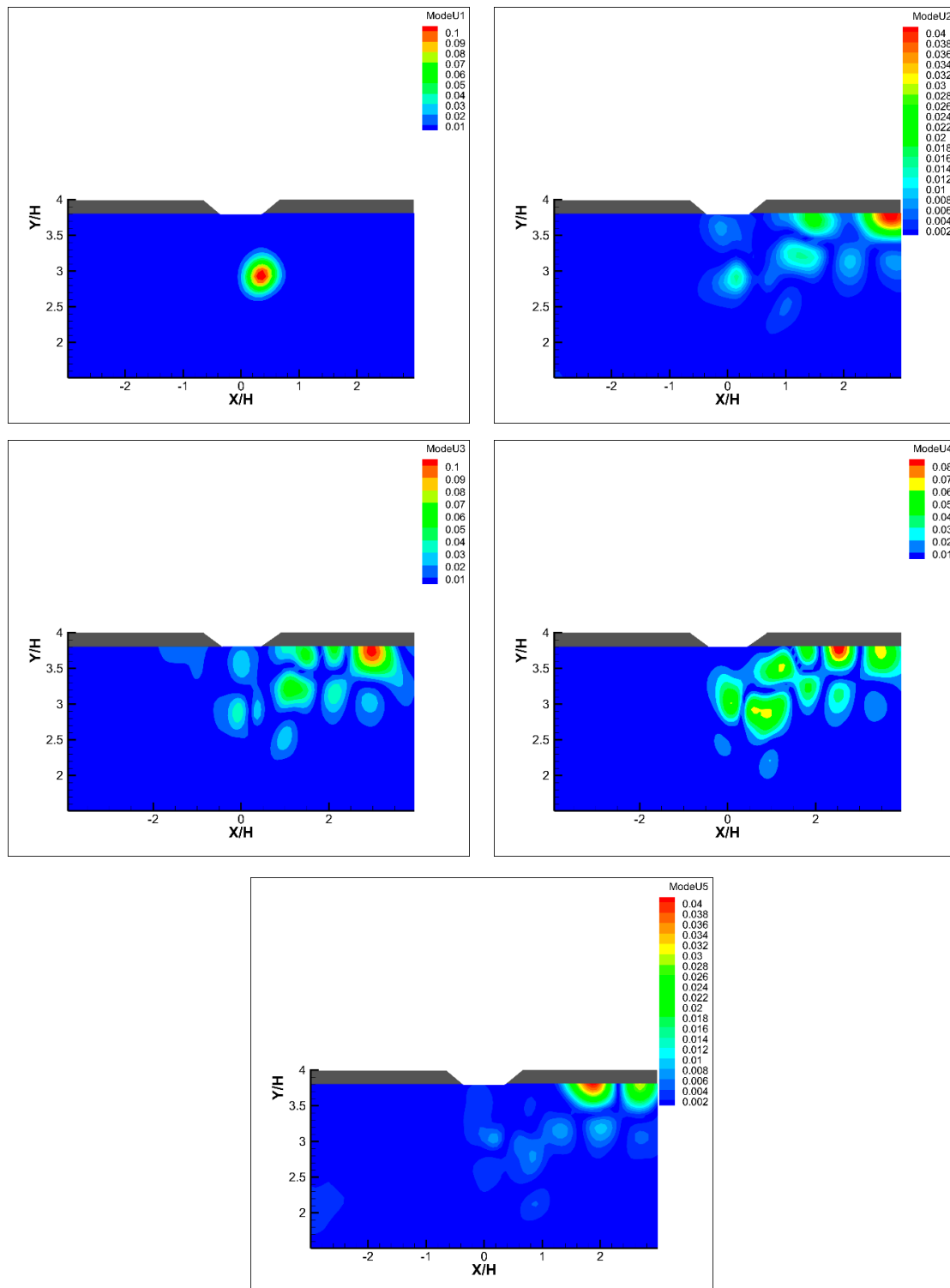


**Figure 12.** The first five highest energy spatial modes of longitudinal velocity ( $U_y$ ), obtained by snapshot POD for  $Re = 6700$  when the rod is at position 2.

The spectrum of the two highest energy temporal modes (obtained by applying FFT to the temporal modes of the longitudinal velocity signal) in the absence of a rod, when the rod is in position 1, and when the rod is in position 2, are shown in Figure 13. In the absence of a rod, the spectra of temporal modes 1 and 2 showed the appearance of frequencies 211.25 Hz and 378.75 Hz, which indicates that these are the frequencies of passage of the high energy vortices. In the presence of a rod at position 1, no frequency appeared in temporal mode 1. However, the results of temporal mode 2 showed a frequency of 480 Hz, which also appeared in the longitudinal velocity spectrum but not in the acoustic spectrum, indicating that this is the frequency of passage of large structures when there is no interaction with the slot, and no acoustic waves are then registered. Finally, when a rod is at position 2, only one frequency of 248.75 Hz, which did not exist in the velocity spectrum nor in the acoustic spectrum, appeared in temporal mode 2. This would indicate that this is the frequency of the creation of vortices that do not interact with the slot and do not pass through the point of extraction of the velocity signal plotted in Figure 7b.

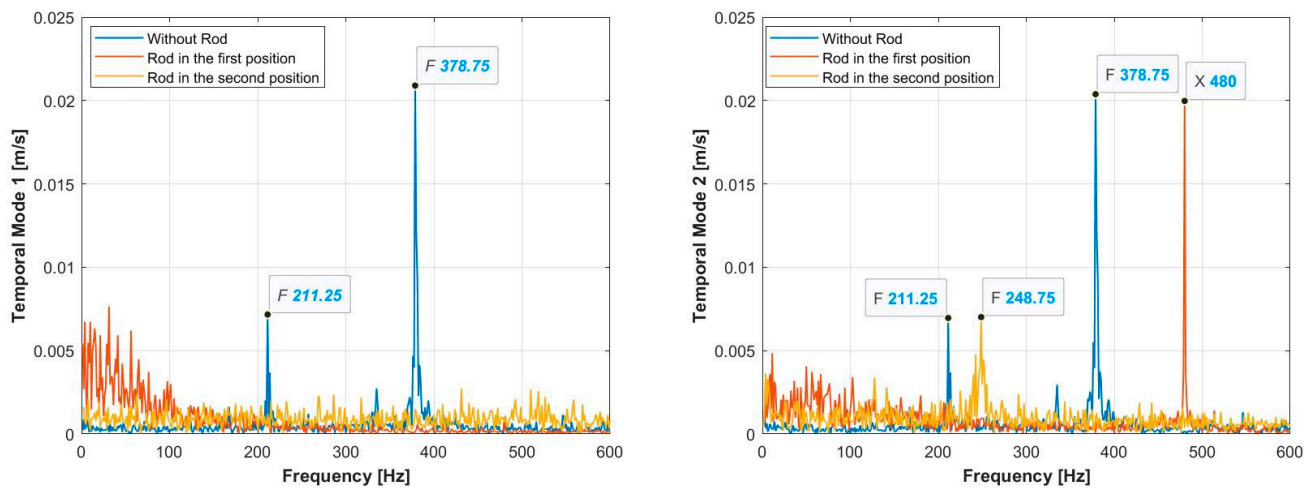


**Figure 13.** Spectral distribution of the two highest energy temporal POD modes for  $Re = 6700$  for all three cases: absence of the rod, presence of the rod at position 1, and presence of the rod at position 2.

#### 4. Discussion

The acoustic map shown in Figure 4 proves that the position of the rod had a significant effect on the control mechanism of noise reduction. However, there are three main regions where sound pressure levels differ notably. The first was located symmetrically beside the jet axis and occupied the zone between  $Y/H = 0$  and  $Y/H = 2.6$ . The presence of a rod in this zone split the main jet into almost two symmetrical jets (as shown by the POD spatial modes in Figure 11). The coherent structures obtained from the two resultant jets hit the plate without passing through the slot, so there was no interaction between the vortices and the slot, which led to a reduction in the SPL. The consequences of this are illustrated by low amplitudes in the acoustic spectrum and the high energy temporal mode of the velocity signal spectrum (shown in Figures 7a and 13, respectively). A second region was located below the first and occupied  $-0.65 < X/H < -0.45$  vertically and  $Y/H = 1.5$  to  $Y/H = 3$  horizontally. When a rod was placed in this region, the main jet was also divided into two jets. Since the zone is not in the axis of symmetry, the two jets were no longer symmetrical with respect to the jet axis (see Figure 8(b3)): the vortices coming from the right jet hit the plate surface without interacting with the slot. Nevertheless, the coherent structures formed in the left jet had the highest energy values (see Figure 12) and passed through the slot without interacting with the borders. This passage produced a broadband noise with high amplitudes, as shown in the acoustic spectrum (Figure 7a), which led to an increase in the SPL. A comparison between these cases and the case without a rod indicated that when the vortices passed totally through the slot (as was the case in the presence of a rod at position 2), the sound was produced with a broadband activity and not with

a specific frequency, as observed when there was no rod. Finally, a third region located outside of the first two regions was also present. Based on the acoustic results, the presence of a rod in this region did not affect the turbulence dynamics since no variation in the SPL was observed.

## 5. Conclusions

The present study was based on the need to dramatically reduce the noise generated by a rectangular jet impinging a slotted plate [19,54,71,72]. This study was carried out on a jet exit at a Reynolds number  $Re = 6700$  and Strouhal number  $St = 0.17$ , and for an impact ratio  $L/H = 4$ . The results showed that the large-scale vortices interacted with the slot and produced acoustic waves that coupled with the aerodynamic modes. Therefore, a passive control mechanism consisting of a rod that strongly affected the vortex dynamics and thus the interaction between the jet and the plate was introduced. Different positions of the rod were tested to find the most effective position of the rod in terms of noise generation. It was found that the rod successfully reduced the noise emitted when it was placed in specific regions between the jet exit and the impinging plate. Dynamically, the rod divided the main jet into two secondary jets: upper and lower jets. The vortices produced from these jets hit the wall without interacting with the slot, which led to the disappearance of the self-sustaining tones and thus a reduction in the sound pressure level to 19 dB. A POD analysis was conducted to better understand the effect of large-scale structures on the generation of self-sustaining tones. The analysis of the POD spectral content and the transversal velocity spectrum revealed details on the role of the large vertical structures in the acoustics and overall noise reduction. This mechanism can be considered as a successful control of the noise of impinging jets when placed between  $Y/H = 0.3$  and  $Y/H = 3$  (the dark blue zone in Figure 4), and it would be interesting to study its performance for other impact ratios and different Reynolds numbers. In addition, one can study the effect of the presence of a rod on the flow rate through the slot to ensure that this control mechanism does not negatively affect the performance of the whole system.

**Author Contributions:** Conceptualization, A.S., M.A., K.A.-M. and H.A.; methodology, A.S., M.A., K.A.-M. and H.A.; software, M.A.; writing—original draft preparation, N.E.A., H.A., B.E.Z. and M.E.H.; writing—review and editing, N.E.A., H.A., B.E.Z. and M.E.H.; project administration, A.S., K.A.-M. and H.A.; and funding acquisition, A.S. All authors have read and agreed to the published version of the manuscript.

**Funding:** This research was funded by FEDER and the region of Nouvelle Aquitaine.

**Data Availability Statement:** The data presented in this study are available on request from the corresponding author. The data are not publicly available due to the Laboratory's privacy policy.

**Conflicts of Interest:** The authors declare no conflict of interest.

## References

1. Vejrazka, J. Experimental Study of a Pulsating Round Impinging Jet. Ph.D. Thesis, INPG, Grenoble, France, 2002. Available online: <https://www.theses.fr/2002INPG0160> (accessed on 12 July 2023).
2. Sondhauss, C. Ueber die beim Ausströmen der Luft entstehenden Töne. *Ann. Phys. Chem.* **1854**, *167*, 126–147. [CrossRef]
3. Rayleigh, J.W. Strutt, Baron. The Theory of Sound, Volume 2. 1986. Available online: <http://archive.org/details/in.ernet.dli.2015.22520> (accessed on 28 February 2020).
4. Powell, A. Theory of Vortex Sound. *J. Acoust. Soc. Am.* **1964**, *36*, 177–195. [CrossRef]
5. Powell, A. The sound-producing oscillations of round underexpanded jets impinging on normal plates. *J. Acoust. Soc. Am.* **1988**, *83*, 515–533. [CrossRef]
6. Powell, A. On Edge Tones and Associated Phenomena. Available online: <https://www.ingentaconnect.com/search/article?option2=author&value2=Powell%252c+Alan&pageSize=10&index=7> (accessed on 28 February 2020).
7. Ho, C.-M.; Nosseir, N.S. Large coherent structures in an impinging turbulent jet. In Proceedings of the 2nd Symposium on Turbulent Shear Flows, London, UK, 2–4 July 1979; pp. 7.26–7.31. Available online: <http://adsabs.harvard.edu/abs/1979stsf.procR...7H> (accessed on 4 April 2017).
8. Powell, A. On the Edgetone. *J. Acoust. Soc. Am.* **1961**, *33*, 395–409. [CrossRef]

9. Lighthill, M.J. On Sound Generated Aerodynamically I. General theory. *Proc. R. Soc. Lond. Ser. Math. Phys. Sci.* **1952**, *211*, 564–587. [[CrossRef](#)]
10. Lighthill, M.J. On sound generated aerodynamically II. Turbulence as a source of sound. *Proc. R. Soc. Lond. A* **1954**, *222*, 1–32. [[CrossRef](#)]
11. Lighthill, M.J. Jet Noise. *AIAA J.* **1963**, *1*, 1507–1517. [[CrossRef](#)]
12. Chanaud, R.C.; Powell, A. Some Experiments concerning the Hole and Ring Tone. *J. Acoust. Soc. Am.* **1965**, *37*, 902–911. [[CrossRef](#)]
13. Rockwell, D.; Naudascher, E. Self-Sustained Oscillations of Impinging Free Shear Layers. *Annu. Rev. Fluid Mech.* **1979**, *11*, 67–94. [[CrossRef](#)]
14. Ho, C.-M.; Nosseir, N.S. Dynamics of an impinging jet. Part 1. The feedback phenomenon. *J. Fluid Mech.* **1981**, *105*, 119. [[CrossRef](#)]
15. Krothapalli, A.; Rajkuperan, E.; Alvi, F.; Lourenco, L. Flow field and noise characteristics of a supersonic impinging jet. *Fluid Mech.* **1999**, *392*, 155–181. [[CrossRef](#)]
16. Zhang, Y. Experimental studies of the turbulence structures of impinging reacting jets using time-resolved particle image velocimetry visualisation, hot wire anemometry and acoustic signal processing. *Exp. Fluids* **2000**, *29*, S282–S290. [[CrossRef](#)]
17. Uzun, A.; Kumar, R.; Hussaini, M.Y.; Alvi, F.S. Prediction of supersonic impinging jet noise using computational aeroacoustics. In Proceedings of the INTER-NOISE, Osaka, Japan, 4–7 September 2011.
18. El Hassan, M.; Assoum, H.H.; Sobolik, V.; Vétel, J.; Abed-Meraïm, K.; Garon, A.; Sakout, A. Experimental investigation of the wall shear stress and the vortex dynamics in a circular impinging jet. *Exp. Fluids* **2012**, *52*, 1475–1489. [[CrossRef](#)]
19. Assoum, H.H.; Hamdi, J.; Abed-Meraïm, K.; El Hassan, M.; Hammoud, A.; Sakout, A. Experimental investigation the turbulent kinetic energy and the acoustic field in a rectangular jet impinging a slotted plate. *Energy Procedia* **2017**, *139*, 398–403. [[CrossRef](#)]
20. Assoum, H.H.; El Hassan, M.; Hamdi, J.; Alkheir, M.; Meraim, K.A.; Sakout, A. Turbulent Kinetic Energy and self-sustaining tones in an impinging jet using High Speed 3D Tomographic-PIV. *Energy Rep.* **2020**, *6*, 802–806. [[CrossRef](#)]
21. Assoum, H.H.; Hamdi, J.; El Hassan, M.; Abed-Meraïm, K.; El Kheir, M.; Mrach, T.; El Asmar, S.; Sakout, A. Turbulent kinetic energy and self-sustaining tones: Experimental study of a rectangular impinging jet using high Speed 3D tomographic Particle Image Velocimetry. *J. Mech. Eng. Sci.* **2020**, *14*, 6322–6333. [[CrossRef](#)]
22. Assoum, H.H.; Hamdi, J.; Alkheir, M.; Abed Meraim, K.; Sakout, A.; Obeid, B.; El Hassan, M. Tomographic Particle Image Velocimetry and Dynamic Mode Decomposition (DMD) in a Rectangular Impinging Jet: Vortex Dynamics and Acoustic Generation. *Fluids* **2021**, *6*, 429. [[CrossRef](#)]
23. Assoum, H.H.; Hamdi, J.; Abed-Meraïm, K.; El Hassan, M.; Ali, M.; Sakout, A. Correlation between the acoustic field and the transverse velocity in a plane impinging jet in the presence of self-sustaining tones. *Energy Procedia* **2017**, *139*, 391–397. [[CrossRef](#)]
24. Assoum, H.H.; Hamdi, J.; Abed-Meraïm, K.; Al Kheir, M.; Mrach, T.; El Soufi, L.; Sakout, A. Spatio-Temporal Changes in the Turbulent Kinetic Energy of a Rectangular Jet Impinging on a Slotted Plate Analyzed with High Speed 3D Tomographic-Particle Image Velocimetry Spatio-Temporal Changes in the Turbulent Kinetic Energy of a Rectangular Jet. *Int. J. Heat Technol.* **2019**, *37*, 1071–1079. [[CrossRef](#)]
25. Schmid, P.J. Dynamic mode decomposition of numerical and experimental data. *J. Fluid Mech.* **2010**, *656*, 5–28. [[CrossRef](#)]
26. Lucas, N.; Doty, M.; Taubert, L.; Wygnanski, I. Reducing the noise emanating from a twin jet nozzle using flexible filaments. *Exp. Fluids* **2013**, *54*, 1504. [[CrossRef](#)]
27. Geyer, T.F. Experimental evaluation of cylinder vortex shedding noise reduction using porous material. *Exp. Fluids* **2020**, *61*, 153. [[CrossRef](#)]
28. Alvi, F.S.; Shih, C.; Elavarasan, R.; Garg, G.; Krothapalli, A. Control of Supersonic Impinging Jet Flows Using Supersonic Microjets. *AIAA J.* **2003**, *41*, 1347–1355. [[CrossRef](#)]
29. Choi, J.J.; Annaswamy, A.M.; Lou, H.; Alvi, F.S. Active control of supersonic impingement tones using steady and pulsed microjets. *Exp. Fluids* **2006**, *41*, 841–855. [[CrossRef](#)]
30. Kopiev, V.F.; Bityurin, V.A.; Belyaev, I.V.; Godin, S.M.; Zaitsev, M.Y.; Klimov, A.I.; Kopiev, V.A.; Moralev, I.A.; Ostrikov, N.N. Jet noise control using the dielectric barrier discharge plasma actuators. *Acoust. Phys.* **2012**, *58*, 434–441. [[CrossRef](#)]
31. Gomez Carrasco, F.J. Matrix-Free Time-Stepping Methods for the Solution of TriGlobal Instability Problems. Ph.D. Thesis, School of Aeronautics, Universidad Politécnica de Madrid, Madrid, Spain, 2013.
32. Dipankar, A.; Sengupta, T.K.; Talla, S.B. Suppression of vortex shedding behind a circular cylinder by another control cylinder at low Reynolds numbers. *J. Fluid Mech.* **2007**, *573*, 171–190. [[CrossRef](#)]
33. Strykowski, P.J.; Sreenivasan, K.R. On the formation and suppression of vortex ‘shedding’ at low Reynolds numbers. *J. Fluid Mech.* **1990**, *218*, 71. [[CrossRef](#)]
34. Favier, J.; Dauptain, A.; Basso, D.; Bottaro, A. Passive separation control using a self-adaptive hairy coating. *J. Fluid Mech.* **2009**, *627*, 451–483. [[CrossRef](#)]
35. Høpfner, J.; Bottaro, A.; Favier, J. Mechanisms of non-modal energy amplification in channel flow between compliant walls. *J. Fluid Mech.* **2010**, *642*, 489–507. [[CrossRef](#)]
36. Skillen, A.; Revell, A.; Pinelli, A.; Piomelli, U.; Favier, J. Flow over a Wing with Leading-Edge Undulations. *AIAA J.* **2015**, *53*, 464–472. [[CrossRef](#)]
37. BenChiekh, M.; Bera, J.-C.; Michard, M.; Sunyach, M. Contrôle par jet pulsé de l’écoulement dans un divergent court à grand angle. *Comptes Rendus Académie Sci. Ser. II B Mech.* **2000**, *328*, 749–756. [[CrossRef](#)]

38. Lecordier, J.C.; Hamma, L.; Paranthoen, P. The control of vortex shedding behind heated circular cylinders at low Reynolds numbers. *Exp. Fluids* **1991**, *10*, 224–229. [[CrossRef](#)]
39. Wan, H.; Patnaik, S.S. Suppression of vortex-induced vibration of a circular cylinder using thermal effects. *Phys. Fluids* **2016**, *28*, 123603. [[CrossRef](#)]
40. Korkischko, I.; Meneghini, J.R. Suppression of vortex-induced vibration using moving surface boundary-layer control. *J. Fluids Struct.* **2012**, *34*, 259–270. [[CrossRef](#)]
41. Patino, G.A.; Gioria, R.S.; Meneghini, J.R. Evaluating the control of a cylinder wake by the method of sensitivity analysis. *Phys. Fluids* **2017**, *29*, 044103. [[CrossRef](#)]
42. Chapin, V.G.; Boulanger, N.; Chassaing, P. Improvement of the jet-vectoring through the suppression of a global instability. In Proceedings of the IUTAM Symposium on Flow Control and MEMS, London, UK, 19–22 September 2026; Morrison, J.F., Birch, D.M., Lavoie, P., Eds.; Springer: Dordrecht, The Netherlands, 2008; Volume 7, pp. 393–396. [[CrossRef](#)]
43. Gioria, R.S.; Jabardo, P.J.S.; Carmo, B.S.; Meneghini, J.R. Floquet stability analysis of the flow around an oscillating cylinder. *J. Fluids Struct.* **2009**, *25*, 676–686. [[CrossRef](#)]
44. Blackburn, H.M.; Sheard, G.J. On quasiperiodic and subharmonic Floquet wake instabilities. *Phys. Fluids* **2010**, *22*, 031701. [[CrossRef](#)]
45. Hill, C. A theoretical approach for analyzing the restabilization of wakes. In Proceedings of the 30th Aerospace Sciences Meeting and Exhibit, Reno, NV, USA, 6–9 January 1992; American Institute of Aeronautics and Astronautics: Reno, NV, USA, 1992; Volume 92.
46. Marquet, O.; Sipp, D.; Jacquin, L. Sensitivity analysis and passive control of cylinder flow. *J. Fluid Mech.* **2008**, *615*, 221–252. [[CrossRef](#)]
47. Pralits, J.O.; Brandt, L.; Giannetti, F. Instability and sensitivity of the flow around a rotating circular cylinder. *J. Fluid Mech.* **2010**, *650*, 513–536. [[CrossRef](#)]
48. Assoum, H. Étude Expérimentale des Couplages Entre La Dynamique d’un Jet Qui Heurte Une Plaque Fendue et L’émission Sonore Générée. Ph.D. Thesis, Université de La Rochelle, La Rochelle, France, 2013.
49. Arroyo, M.P.; Greated, C.A. Stereoscopic particle image velocimetry. *Meas. Sci. Technol.* **1991**, *2*, 1181. [[CrossRef](#)]
50. Calluaud, D.; David, L. Stereoscopic particle image velocimetry measurements of the flow around a surface-mounted block. *Exp. Fluids* **2004**, *36*, 53–61. [[CrossRef](#)]
51. Watanabe, R.; Gono, T.; Yamagata, T.; Fujisawa, N. Three-dimensional flow structure in highly buoyant jet by scanning stereo PIV combined with POD analysis. *Int. J. Heat Fluid Flow* **2015**, *52*, 98–110. [[CrossRef](#)]
52. Wieneke, B. Volume self-calibration for 3D particle image velocimetry. *Exp. Fluids* **2008**, *45*, 549–556. [[CrossRef](#)]
53. Kähler, C.J.; Kompenhans, J. Fundamentals of multiple plane stereo particle image velocimetry. *Exp. Fluids* **2000**, *29*, S070–S077. [[CrossRef](#)]
54. Alkheir, M.; Assoum, H.H.; Afyouni, N.E.; Abed Meraim, K.; Sakout, A.; El Hassan, M. Combined Stereoscopic Particle Image Velocimetry Measurements in a Single Plane for an Impinging Jet around a Thin Control Rod. *Fluids* **2021**, *6*, 430. [[CrossRef](#)]
55. Raffel, M.; Willert, C.; Scarano, F.; Christian, K.; Wereley, S.; Kompenhans, J. Particle Image Velocimetry: A Practical Guide (PDF Download Available), SpringerLink. Available online: <https://link.springer.com/book/10.1007/978-3-319-68852-7> (accessed on 3 April 2018).
56. Chen, Q.; Zhong, Q.; Qi, M.; Wang, X. Comparison of vortex identification criteria for planar velocity fields in wall turbulence. *Phys. Fluids* **2015**, *27*, 085101. [[CrossRef](#)]
57. Jeong, J.; Hussain, F. On the identification of a vortex. *J. Fluid Mech.* **1995**, *285*, 69–94. [[CrossRef](#)]
58. Miron, P.; Vétel, J.; Garon, A.; Delfour, M.; Hassan, M.E. Anisotropic mesh adaptation on Lagrangian Coherent Structures. *J. Comput. Phys.* **2012**, *231*, 6419–6437. [[CrossRef](#)]
59. Berkooz, G.; Holmes, P.; Humley, J.L. The Proper Orthogonal Decomposition in the Analysis of Turbulent Flows. *Ann. Rev. Fluid Mech.* **1993**, *25*, 539–575. [[CrossRef](#)]
60. Chatterjee, A. An Introduction to the Proper Orthogonal Decomposition. *Curr. Sci.* **2000**, *10*, 808–817.
61. Pedersen, J.; Meyer, K. POD analysis of flow structures in a scale model of a ventilated room. *Exp. Fluids* **2002**, *33*, 940–949. [[CrossRef](#)]
62. Kostas, J.; Soria, J.; Chong, M.S. A comparison between snapshot POD analysis of PIV velocity and vorticity data. *Exp. Fluids* **2005**, *38*, 146–160. [[CrossRef](#)]
63. Hammad, K.J.; Milanovic, I.M. A POD study of an impinging jet flowfield. In Proceedings of the Fluids Engineering Division Summer Meeting, Vail, CO, USA, 2 August 2009; Volume 1: Symposia, Parts A, B and C; ASME: Vail, CO, USA, 2009; pp. 1477–1485. [[CrossRef](#)]
64. Podvin, B.; Sergent, A. Proper orthogonal decomposition investigation of turbulent Rayleigh-Bénard convection in a rectangular cavity. *Phys. Fluids* **2012**, *24*, 105106. [[CrossRef](#)]
65. Graftieaux, L.; Michard, M.; Grosjean, N. Combining PIV, POD and vortex identification algorithms for the study of unsteady turbulent swirling flows. *Meas. Sci. Technol.* **2001**, *12*, 1422. [[CrossRef](#)]
66. Vernet, R.; Thomas, L.; David, L. Analysis and reconstruction of a pulsed jet in crossflow by multi-plane snapshot POD. *Exp. Fluids* **2009**, *47*, 707. [[CrossRef](#)]

67. Bernero, S.; Fiedler, H.E. Application of particle image velocimetry and proper orthogonal decomposition to the study of a jet in a counterflow. *Exp. Fluids* **2000**, *29*, S274–S281. [[CrossRef](#)]
68. Delville, J. Characterization of the organization in shear layers via the Proper Orthogonal Decomposition. *Appl. Sci. Res.* **1994**, *53*, 263–281. [[CrossRef](#)]
69. Zhang, Q.; Liu, Y.; Wang, S. The identification of coherent structures using proper orthogonal decomposition and dynamic mode decomposition. *J. Fluids Struct.* **2014**, *49*, 53–72. [[CrossRef](#)]
70. Druault, P.; Guibert, P.; Alizon, F. Use of proper orthogonal decomposition for time interpolation from PIV data. *Exp. Fluids* **2005**, *39*, 1009–1023. [[CrossRef](#)]
71. Hamdi, J.; Assoum, H.H.; Alkheir, M.; Abed-Meraïm, K.; Cauet, S.; Sakout, A. Analysis of the 3D flow of an impinging jet on a slotted plate using TR-Tomo PIV and Proper Orthogonal Decomposition. *Energy Rep.* **2020**, *6*, 158–163. [[CrossRef](#)]
72. Hamdi, J.; Assoum, H.; Abed-Meraïm, K.; Sakout, A. Analysis of the effect of the 3C kinematic field of a confined impinging jet on a slotted plate by stereoscopic PIV. *Eur. J. Mech. B Fluids* **2019**, *76*, 243–258. [[CrossRef](#)]

**Disclaimer/Publisher’s Note:** The statements, opinions and data contained in all publications are solely those of the individual author(s) and contributor(s) and not of MDPI and/or the editor(s). MDPI and/or the editor(s) disclaim responsibility for any injury to people or property resulting from any ideas, methods, instructions or products referred to in the content.